Three-dimensional registration of synchrotron radiation-based micro-computed tomography images with advanced laboratory micro-computed tomography data from murine kidney casts

Peter Thalmann[a], Simone E. Hieber[a], Georg Schulz[a], Hans Deyhle[a], Anna Khimchenko[a], Vartan Kurtcuoglu[b], Ufuk Olgac[b], Anastasios Marmaras[b], Willy Kuo[b], Eric P. Meyer[c], Felix Beckmann[d], Julia Herzen[e], Stefanie Ehrbar[a] and Bert Müller[a]

[a]Biomaterials Science Center, University of Basel, 4031 Basel, Switzerland;
[b]Institute of Physiology, University of Zurich, 8057 Zurich, Switzerland;
[c]Institute of Molecular Life Sciences, University of Zurich, 8057 Zurich, Switzerland;
[d]Institute of Materials Research, Helmholtz-Zentrum Geesthacht, 21502 Geesthacht;
[e]Department of Physics, Technical University of Munich, 85748 Garching, Germany

ABSTRACT

Malfunction of oxygen regulation in kidney and liver may lead to the pathogenesis of chronic diseases. The underlying mechanisms are poorly understood. In kidney, it is hypothesized that renal gas shunting from arteries to veins eliminates excess oxygen. Such shunting is highly dependent on the structure of the renal vascular network. The vascular tree has so far not been quantified under maintenance of its connectivity as three-dimensional imaging of the vessel tree down to the smallest capillaries, which in mouse model are smaller than 5 µm in diameter, is a challenging task. An established protocol uses corrosion casts and applies synchrotron radiation-based micro-computed tomography (SRµCT), which provides the desired spatial resolution with the necessary contrast. However, SRµCT is expensive and beamtime access is limited. We show here that measurements with a phoenix nanotom®m (General Electric, Wunstorf, Germany) can provide comparable results to those obtained with SRµCT, except for regions with small vessel structures, where the signal-to-noise level was significantly reduced. For this purpose the nanotom®m measurement was compared with its corresponding measurement acquired at the beamline P05 at PETRA III at DESY, Hamburg, Germany.

Keywords: post mortem imaging, computed microtomography, vessel microstructures, vascularization, capillaries, morphology, osmium staining, registration

1. INTRODUCTION

Chronic kidney disease (CKD) is a major and worldwide public health problem with a high and rising prevalence, with more than 26 million cases in adults within the United States according to the National Kidney Foundation [1]. Patients with CKD suffer from deteriorating kidney function to the point of renal failure and are at high risk for cardiovascular mortality [2]. Hypoxia has been identified as a factor in pathogenesis and progression of CKD and acute kidney injury [3, 4]. To identify the most effective strategies for the treatment of hypoxia, we intend to use computational modeling based on three-dimensional images of the kidney vascular structure to simulate the effects of various parameters (e.g., renal blood flow rate, oxygen consumption and hematocrit) on renal oxygenation. This, however, requires a detailed and complete image of the vessel tree down to the smallest capillaries, which in the mouse model are smaller than 5 µm in diameter.

As the absorption coefficient of a blood vessel is almost equal the one of its surrounding tissues, the contrast provided by synchrotron radiation-based micro-computed tomography (SRµCT) in conventional absorption-contrast mode is poor and a segmentation of the blood vessels is challenging. Other methods such as magnetic

---

resonance tomography and grating-based phase-contrast computed tomography do not yet provide the necessary spatial resolution. A possible alternative could be to use single-distance inline phase-contrast tomography and use a reconstruction algorithm developed by Paganin et al. [5]. However, proof whether the latter method is able of providing the necessary contrast for the segmentation of the smallest capillaries does not yet exist. An established protocol for investigating kidney vasculature is vascular corrosion casting [6], in which the blood vessels of the organism of interest are perfused with a hardening material, typically a plastic resin. The surrounding tissues can then be removed by corroding with a potassium hydroxide solution, allowing imaging of the blood vessel casts with scanning electron microscopy (SEM) or similar. While SEM is capable of acquiring very detailed pictures of the cast surfaces [7], it does not confer true 3D data and can not image obstructed deeper regions of a tissue. Recently, it has been shown that with low photon energy, below 20 keV, corrosion casts can also be used for SRµCT [8–12]. Since it produces high-resolution three-dimensional images, SRµCT presents itself as an excellent alternative if such data is required. However, SRµCT is expensive and beamtime access is limited. Therefore we intend to show here the potential of high-resolution laboratory CT-scanners as a complementary approach to absorption-based computed-tomography at synchrotron facilities in the low photon energy range. Comparison of this kind have already been made [13], but only for photon energies considerably higher than in this study.

2. METHODS

2.1 Specimen preparation

A balb/c nude mouse (Charles River Laboratories, France) weighting 24 g at an age of 10 weeks were used for the casting. Approval was obtained from the cantonal ethics committee and the experiment was performed in strict adherence to the Swiss law for animal protection. The mouse was casted according to the procedure described by Krucker et al. [7]. Thus, the mouse was anaesthetized with a penobarbital and perfused through the left ventricle of the heart with 10 ml PBS with Heparin (25000 units / l), then with 10 ml formaldehyde solution 4 % and finally with 10 ml of polyurethane PU4ii-mixture (vasQtec, Switzerland). The resin was left to cure for several days, and then the body was corroded in a bath of 10 % potassium hydroxide solution at 55 °C. Any remaining bone was removed with 5 % formic acid solution and the left over plastic cast washed with water, freeze-dried, and then osmium coated for enhanced contrast.

It is important that the specimen undergoes as few deformations as possible during measurement. For that purpose the sample was fixed within a cylindric straw allowing alignment over multiple height steps, which is advantageous when height steps have to be merged.

2.2 Synchrotron radiation-based micro-computed tomography

The absorption contrast-based SRµCT was carried out at the beamline P05 at the DESY PETRA III storage ring operated by the Helmholtz-Zentrum Geesthacht [14]. The photon energy was set to 9 keV with the help of a double crystal monochromator (Si-crystall with Bragg modes 111 and 311). During the measurement 1800 projections with equidistant angular position over 360° were acquired with an asymmetric rotation axis [15]. Images were acquired with a CCD-camera with 3056 x 3056 pixels and a magnification of 10.453 resulting in a field of view of 3.508 mm x 3.508 mm and an effective pixel size of 1.148 µm respectively.

In order to obtain a comparable pixel size with the nanotom measurement, the tomographic data sets were reconstructed with a binning factor of 2. A filtered back-projection algorithm was used for the reconstruction implemented in Matlab ®(2014a, The MathWorks, Natick, USA). Due to the huge size of the data sets the GPU implementation of the inverse radon transform – iradon.m – was used with a linear interpolator and a Ram-Lak filter. The evaluation of the correct flat-field necessary for the beamline P05 is described by S.E. Hieber et al. [16].

2.3 Nanotom

The phoenix nanotom®m (General Electric, Wunstorf, Germany) is an X-ray tube-based high-resolution CT system with cone-beam geometry and transmission source. It is equipped with a 15 – 180 kV X-ray source with up to 200 nm detail detectability and internal cooling – optimized for long-term stability [17] – and is operated with a tungsten or a molybdenum target. Since corrosion casts exhibit low X-ray attenuation, the molybdenum
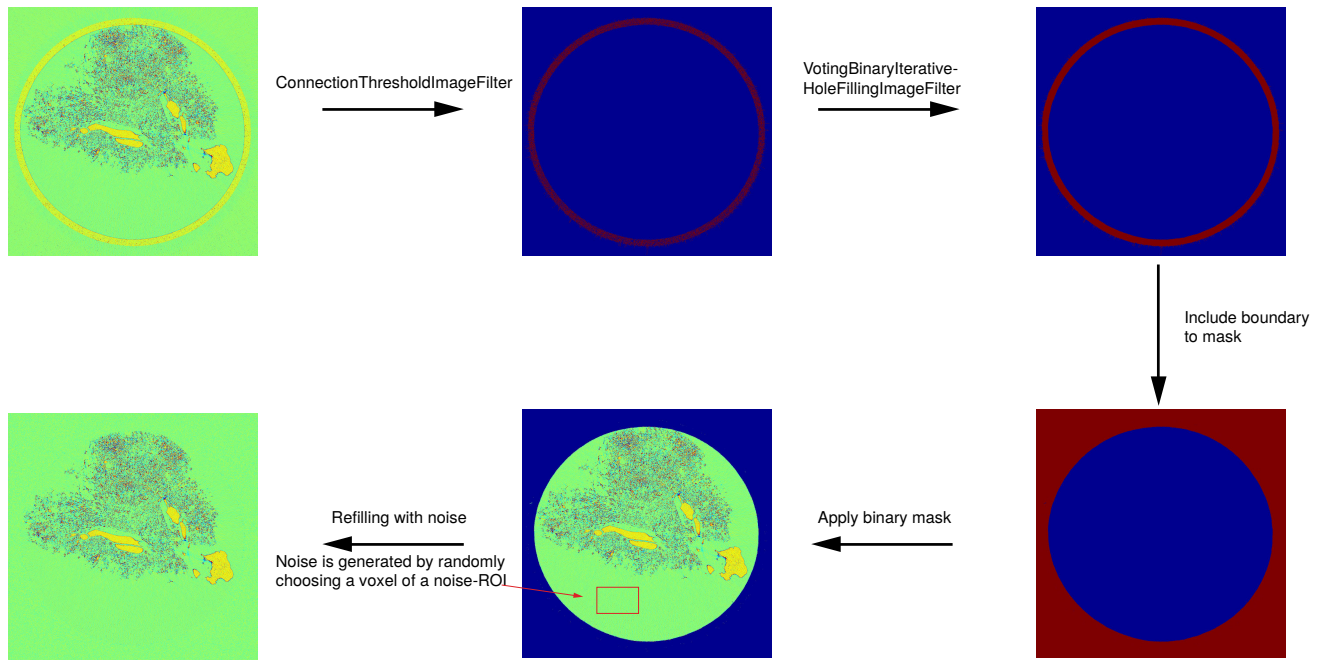
Figure 1: Illustration of the segmentation process performed to remove the straw from the data sets for registration purposes. The filters used are available in the open-source library provided by the National Library of Medicine Insight Segmentation and Registration Toolkit (ITK) [22].

target was chosen for the measurement, as the high dose in the bremstrahlung characteristic of the target has a lower photon energy compared to tungsten. The acceleration voltage was set to 40 kV, and the beam current to 230 µA. Lower acceleration voltges gave rise to a beam with insufficient photon flux. The 1401 projections, acquired over 360°, resulted in images with an effective pixel size of 2.5 µm, which is significantly smaller than in previous studies [18–20], especially with regard to the objective of visualizing the smallest capillaries. For each projection 10 images where acquired with an exposure time of 1 s each and averaged. The tube operation mode was 0, which corresponds, according to the manufacturer, to a focal spot size of 2.7 µm. This was the maximal source size possible for our setup and was still sufficient for our experiment.

The reconstruction was performed with the software phoenix datos x 2.0.1 - RTM (GE Sensing & Inspection Technologies GmbH, Wunstorf, Germany). The implementation of the reconstruction is based on Feldkamps cone-beam reconstruction approach [21]. For optimization, the reconstruction software includes several tools for artifact removal including drift and beam hardening correction.

2.4 Registration

Registration of the data sets is indispensable for direct comparison. During the transport between the two measurements the sample was exposed to shocks and vibrations, which caused small deformations and relative rotations of the sample around the axis perpendicular to the main axis of the specimen container. The volume of the container was large compared to that of the specimen and therefore became dominant in the registration process. Thus, the straw had to be artificially removed from the data in order the get reasonable results in the registration process [9]. For low photon energies, the absorption coefficient of the straw is almost equal to the one of the specimen and therefore prevented segmentation by thresholding. However, slices where the specimen touches the container wall were rare. Furthermore, edge enhancement effects clearly outlined the container border. Thus, a slice-wise region-growing algorithm with a specific adjusted range was able to capture most, but not all points within the straw. The missing pixels were then found by a smart hole-filling algorithm, provided by the open-source library Insight Segmentation and Registration Toolkit [22] (ITK / VotingBinaryIterativeHole-FillingImageFilter). The filter was executed from Matlab by the help of the open-source software gerardus [23].
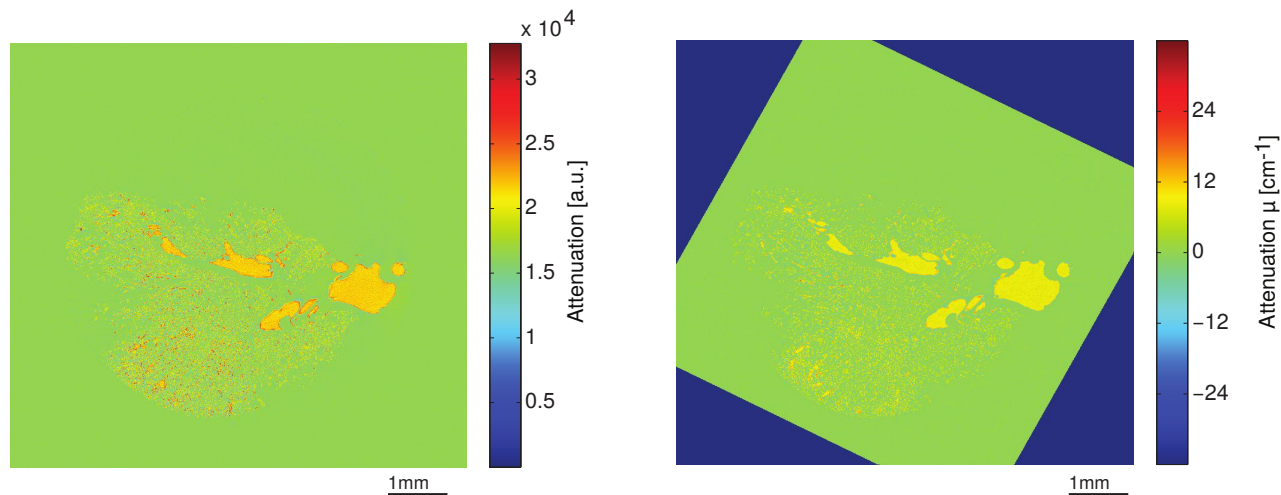
Figure 2: A selected slice of the nanotom reconstruction (left) after a post reconstruction binning with a binning factor of 4 and the corresponding SRµCT-slice (right) after rigid registration.

The straw and all the exterior pixels were replaced by background noise. Therefore, we chose a small region within the straw that did not contain the sample. The histogram then gave the probability-distribution for the random number selection within the spectrum of the noise. A schematic of the straw removal is displayed in Figure 1.

After the removal of the straw, a section of the SRµCT-measurement was intensity-mapped on the nanotom measurement by means of rigid registration. The sectioning was necessary since registration is a time-consuming process and could take weeks with data sets several hundred gigabytes large. Nevertheless, the section is assumed to be large enough to make a qualitative statement. The program used was developed in-house [24] and was executed using the cross-correlation metric and the trilinear interpolation.

3. RESULTS AND DISCUSSION

To assess whether both SRµCT and X-ray tube data sets yield the same amount of cast material, we compared the area below the Gaussian related to the respective material in the histogram of the respective data sets. Because of the huge size of the data sets, we restrict ourselves only on a region of interest (ROI) and not on the whole three-dimensional image. To select a common volume, three-dimensional rigid registration of data sets was performed where the specimen container was artificially removed, see Section 2.4. For ease of handling the ROIs were binned by a factor of 4 before registration. The post reconstructed binned data sets were only used for this specific kind of analysis. Histogram distortion by interpolation was prevented by using nearest-neighbor interpolation. Figure 2 shows a slice of the nanotom tomogram and the corresponding slice of the SRµCT after rigid registration. The fitted histograms are displayed in a semi-logarithmic plot in Figure 3 and the corresponding fitting parameters are listed in Table 1. The histograms in Figure 3 contain only voxels of a region with high specimen prevalence. This has only demonstrative effect, as the ratio of the two Gaussian peaks could be kept small.

Fitting was performed with the software pro Fit 6.2.14 (QuantumSoft, Bühlstrasse 18,8707 Uetikon am See, Switzerland). Advanced laboratory micro-computed tomography was performed with a polychromatic beam, and therefore did not yield fully quantitative attenuation coefficients. For comparison reasons the histogram of the nanotom measurement was scaled such that the two air-peaks coincide (cf. Figure 3). Both histograms could not be fitted by the ansatz of two Gaussians as they strongly deviate from such a theoretical situation. Partial volume effects are prominent because of the high surface-to-volume ratio due to the presence of numerous thin vessels the sample did consist of, and edge enhancement occurs due to phase propagation. Both phenomena contribute to the deviation from the theoretical Gaussian shape of the peaks. Determination of the cast-volume

Table 1: Fitting parameters used for the Gaussian fitting $f(x) = A * \exp\left(\frac{(x-x_0)^2}{2*s^2}\right)$ of the histograms in Figure 3

Cast	A	x_0	s
Nanotom	775.33 ± 1.29	12.49 ± 0.006	2.56 ± 0.01
SRμCT	1036.34 ± 1.42	8.83 ± 0.006	1.87 ± 0.01
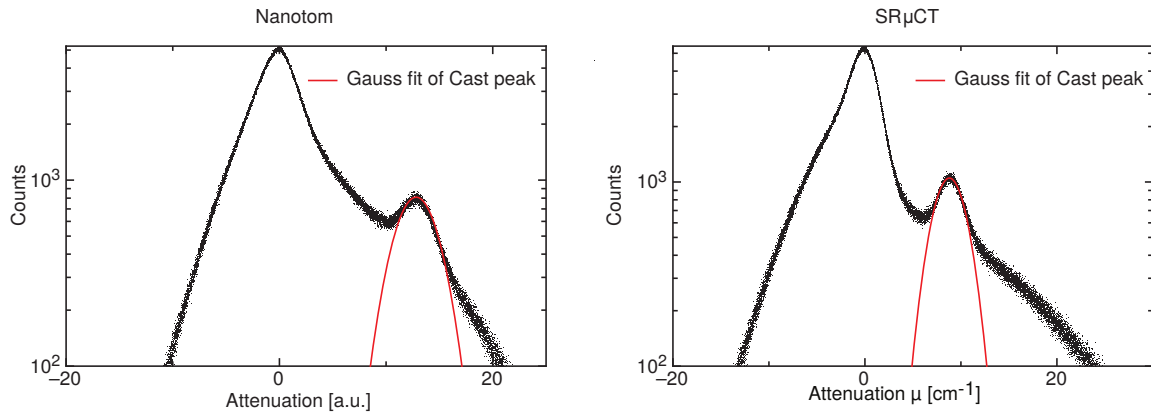
Figure 3: Fitted histogram of a distinct section of the nanotom measurement (left) and of the corresponding SRμCT-histogram (right) after registration.
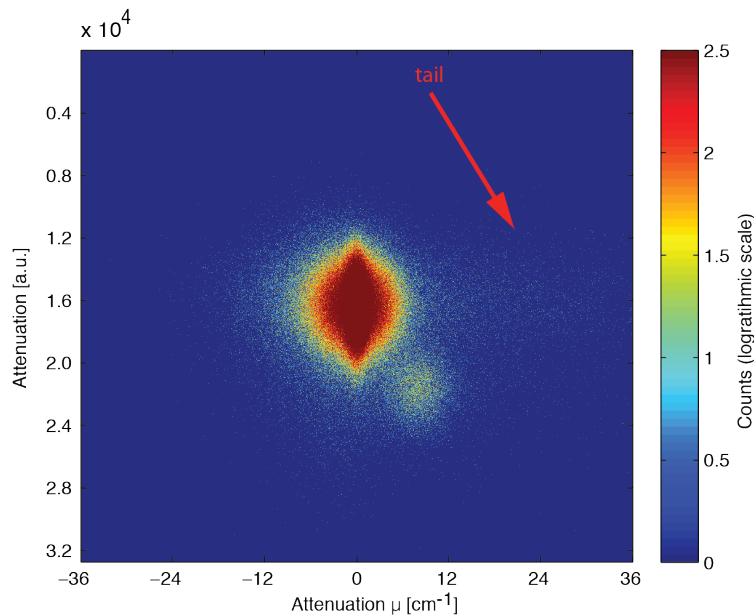
Figure 4: Joint-histogram of a selected region after rigid registration with the SRμCT-measurement as a float
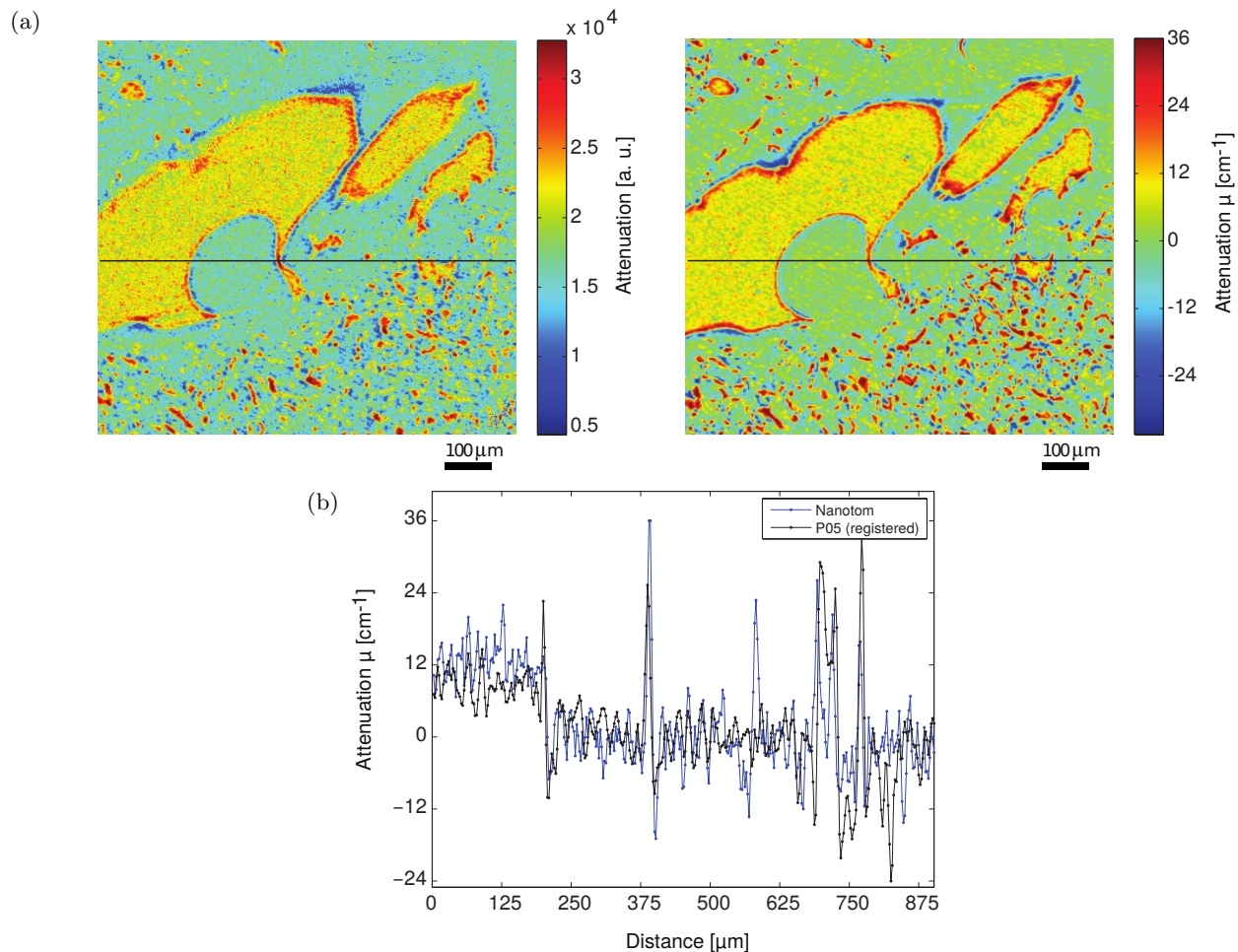
Figure 5: (a) shows a section from a two dimensional slice of the nanotom measurement (left) and the SRµCT-measurement (right) after rigid registration. A line plot of the black line is displayed in (b).

by using the fitting parameters in Table 1 resulted in a cast-volume of 0.2 % ± 1.5 % larger for the SRµCT measurement. However, due to deviation from a Gaussian behavior, the results only serve as an indication and values should not be considered as absolute.

The findings can also be detected in the joint-histogram. In the following we used a smaller ROI than in the histogram analysis, but without post-reconstruction binning - meaning without the execution of a mean-filter. Figure 4 shows the joint-histogram of a smaller selected region - only 500 µm in height - where the SRµCT-image was mapped on the nanotom data by rigid registration using trilinear interpolation. The final similarity value was 0.122316. One can clearly identify two peaks, surrounded by scattering, and a tail, running horizontally from the center of the image to the right border. The small counts within the tail indicate that some vessels that could be visualized by SRµCT but not with the nanotom®-CT system are present. The scattering originates from imperfect registration, as shown in Figure 5a. The specimen underwent a slight deformation between scans, due to commotion during transport. However, the casts are elastic and therefore the external influences while transporting could have also caused a small distortion of the specimen. In such a case vessels with a larger volume are dominant in the registration process and cause an improper mapping of the smaller ones, as can be seen in Figure 5a. Therefore a comparison of such dislocated vessels is an extremely difficult task and for further three dimensional analysis non-rigid registration needs to be taken into consideration. A line plot through a region with reasonable registration and a smaller feature is shown in Figure 5b. The line plots show two almost identical profiles. The spatial resolution is almost identical for both profiles. Furthermore, the signal-to-noise
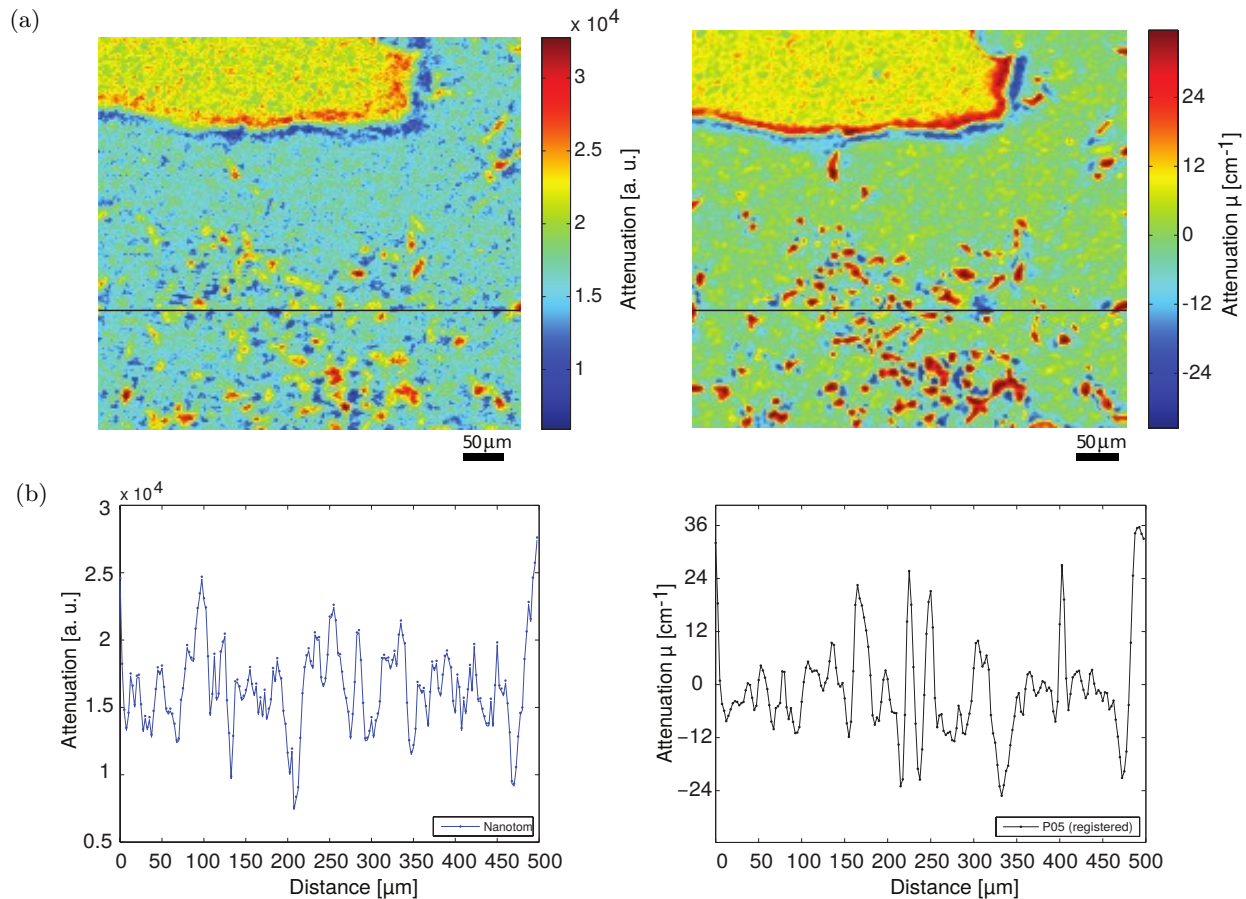
Figure 6: (a) shows a section from a two dimensional slide of the nanotom measurement (left) and the SRµCT-measurement (right) after rigid registration. A line plot of the black line is displayed in (b).

ratio is high for both measurements, but slightly lower in the nanotom measurement. This is partially due to the strong edge enhancement present in the SRµCT data. Even though edge enhancement is favorable to vessel segmentation, it also causes an artificial magnification of the objects, which makes the determination of vessel sizes challenging.

Figure 6a suggests lower contrast of the nanotom-data sets in regions with numerous small vessels. If we compare the line plot of the SRµCT-slices in Figure 5b and Figure 6b, we can see a small loss in the signal-to-noise ratio as more noise is present in regions with a high number of small vessels. Nevertheless, the signal-to-noise ratio is still high, favorable for the segmentation, which is necessary for the characterization of the specimen's vessel structure. In contrast, the nanotom line plot shows only weak signal, which is expected to be caused by photons with higher energies. The peaks from the vessels are still distinguishable from the noise, but segmentation is challenging. Furthermore, manual investigation of individual vessels allowed for the the detection of missing vessels as indicated by Figure 4. However, due to the distortion of the sample a quantitative analysis regarding the missing vessel was not yet possible. As oxygen regulation occurs mainly at the smallest capillaries, it is of great importance to resolve this isssue before advanced labarotory X-ray sources are used for the characterization of the complete vessel structures. A target with a more appropriate bremstrahlung characteristic, e.g. a copper target, which was not available in our lab, is expected to improve the laboratory data.

Spatial resolution estimation by means of Fourier analysis as described in [25], resulted in a spatial resolution of 2.48 µm ± 0.5 µm for the SRµCT and of 5.53 µm ± 0.5 µm for the laboratory µCT.

4. CONCLUSIONS

Despite its broad energy spectrum, the nanotom®-CT system allowed for the visualization of the low X-ray absorbing specimen with high precision. The images obtained from the nanotom®-CT system were comparable to those achieved with SRµCT at the beamline P05 at the DESY PETRA III storage ring. For regions with small vessel structures, the signal-to-noise level was significantly reduced for the X-ray tube data. It is expected that results can be improved by a more appropriate setup, e.g, a copper-target.

It is unclear to what extent advanced lab-source µCT is able to visualize the smallest capillaries. A direct comparison with SRµCT data allows to assess the precision of the conventional µCT, and therefore to investigate the statistical negligibility of missing or incomplete vessels. However, since the corrosion casts are elastic and even slight external influence may alter the shape, rigid image registration is capable of matching only large vessels. For a direct comparison of the smaller vessels non-rigid registration needs to be taken into consideration.

4.1 Acknowledgments

REFERENCES

[1] National Kidney Foundation, I., "About chronic kidney disease," (2014). `http://www.kidney.org/kidneydisease/aboutckd.cfm`.

[2] Herzog, C. A., Asinger, R. W., Berger, A. K., Charytan, D. M., Diez, J., Hart, R. G., Eckardt, K.-U., Kasiske, B. L., McCullough, P. A., Passman, R. S., DeLoach, S. S., Pun, P. H., and Ritz, E., "Cardiovascular disease in chronic kidney disease. a clinical update from kidney disease: Improving global outcomes (kdigo)," *Kidney Int.* **80**(6), 572–586 (2011).

[3] Brezis, M. and Rosen, S., "Mechanisms of disease: Hypoxia of the renal medulla — its implications for disease," *N. Engl. J. Med.* **332**, 647–655 (1995).

[4] Eckardt, K.-U., Bernhardt, W. M., Weidemann, A., Warnecke, C., Rosenberger, C., Wiesener, M. S., and Willam, C., "Role of hypoxia in the pathogenesis of renal disease," *Kidney Int.* **68**, S46–S51 (Dec. 2005).

[5] Paganin, D., Mayo, S. C., Gureyev, T. E., Miller, P. R., and Wilkins, S. W., "Simultaneous phase and amplitude extraction from a single defocused image of a homogeneous object," *J. Microscopy* **206**(1), 33–40 (2002).

[6] Bowman, W., "On the structure and use of the malpighian bodies of the kidney, with observations on the circulation through that gland," *Phil. Trans. R. Soc. Lond.* **132**, 57–80 (1842).

[7] Krucker, T., Lang, A., and Meyer, E. P., "New polyurethane-based material for vascular corrosion casting with improved physical and imaging characteristics," *Microsc. Res. Tech.* **69**(2), 138–147 (2006).

[8] Lang, S., Müller, B., Dominietto, M. D., Cattin, P. C., Zanette, I., Weitkamp, T., and Hieber, S. E., "Three-dimensional quantification of capillary networks in healthy and cancerous tissues of two mice," *Microvascular Res.* **84**(3), 314 – 322 (2012).

[9] Müller, B., Lang, S., Beckmann, F., Dominietto, M., Rudin, M., Zanette, I., Weitkamp, T., Rack, A., and Hieber, S. E., "Comparing the micro-vascular structure of cancerous and healthy tissues," *Proc. SPIE* **8506**, 850607 (2012).

[10] Lang, S., Dominietto, M., Cattin, P., Ulmann-Schuler, A., Weitkamp, T., and Müller, B., "Global and local hard x-ray tomography of a centimeter-size tumor vessel tree," *J. Synchrotron Radiation* **19**(1), 114–125 (2012).

[11] Lang, S., Dominietto, M., and Müller, B., "Visualization of tumor vessels using synchrotron radiation-based micro computed tomography," *J. Phys.: Conference Series* **186**(1), 012088 (2009).

[12] Heinzer, S., Krucker, T., Stampanoni, M., Abela, R., Meyer, E. P., Schuler, A., Schneider, P., and Müller, R., "Hierarchical microimaging for multiscale analysis of large vascular networks," *NeuroImage* **32**(2), 626–636 (2006).

[13] Brunke, O., Brockdorf, K., Drews, S., Müller, B., Donath, T., Herzen, J., and Beckmann, F., "Comparison between x-ray tube-based and synchrotron radiation-based μct," *Proc. SPIE* **7078**, 70780U (2008).

[14] Haibel, A., Beckmann, F., Dose, T., Herzen, J., Ogurreck, M., Müller, M., and Schreyer, A., "Latest developments in microtomography and nanotomography at Petra III," *Powder Diff.* **25**(Special Issue 02), 161–164 (2010).

[15] Müller, B., Bernhardt, R., Weitkamp, T., Beckmann, F., Bräuer, R., Schurigt, U., Schrott-Fischer, A., Glueckert, R., Ney, M., Beleites, T., Jolly, C., and Scharnweber, D., "Morphology of bony tissues and implants uncovered by high-resolution tomographic imaging," *Int. J. Mater. Res.* **98**(7), 613–621 (2007).

[16] Hieber, S. E., Khimchenko, A., Kelly, C., Mariani, L., Thalmann, P., Schulz, G., Schmitz, R., Greving, I., Dominietto, M., and Müller, B., "Three-dimensional imaging of human hippocampal tissue using synchrotron radiation- and grating-based micro computed tomography," *Proc. SPIE* **9212**, 92120S (2014).

[17] GE Measurment & Control, "phoenix nanotom m," (2014). `http://www.ge-mcs.com/en/radiography-x-ray/ct-computed-tomography/phoenix-nanotom-m.html`.

[18] Garcia-Sanz, A., Rodriguez-Barbero, A., Bentley, M. D., Ritman, E. L., and Romero, J. C., "Three-dimensional microcomputed tomography of renal vasculature in rats," *Hypertension* **31**(1), 440–444 (1998).

[19] Nordsletten, D. A., Blackett, S., Bentley, M. D., Ritman, E. L., and Smith, N. P., "Structural morphology of renal vasculature," *Am. J. Physiol. - Heart and Circulatory Physiol.* **291**(1), H296–H309 (2006).

[20] Wagner, R., Van Loo, D., Hossler, F., Czymmek, K., Pauwels, E., and Van Hoorebeke, L., "High-resolution imaging of kidney vascular corrosion casts with nano-ct," *Microscopy and Microanalysis* **17**(02), 215–219 (2011).

[21] Feldkamp, L. A., Davis, L. C., and Kress, J. W., "Practical cone-beam algorithm," *J. Opt. Soc. Am. A* **1**(6), 612–619 (1984).

[22] The Insight Segmentation and Registration Toolkit (2014). `www.itk.org`.

[23] gerardus – Computational biology and medical image processing scripts and programs (2014). `https://code.google.com/p/gerardus`.

[24] Andronache, A., "Multi-modal non-rigid registration of volumetric medical images," *Information technology and electrical engineering, ETH Zurich, No. 16601* (2006).

[25] Schulz, G., Weitkamp, T., Zanette, I., Pfeiffer, F., Müller-Gerbl, M., David, C., and Müller, B., "Asymmetric rotational axis reconstruction of grating-based x-ray phase contrast tomography of the human cerebellum," *Proc. SPIE* **8506**, 850604 (2012).